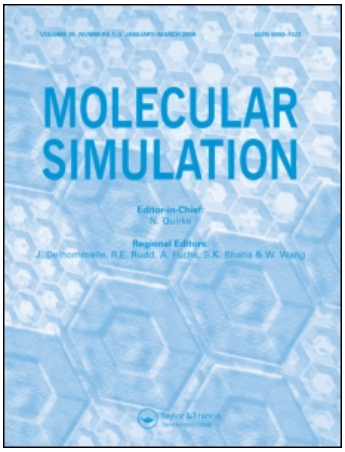

Molecular Simulation
Publication details, including instructions for authors and subscription information:
http://www.informaworld.com/smpp/title~content=t713644482

Computer Simulation of Isothermal Mass Transport in Graphite Slit Pores

Karl P. Travis[a]; Keith E. Gubbins[b]
[a] Department of Chemical and Forensic Sciences, University of Bradford, Bradford, UK [b] Department of Chemical Engineering, Riddick Labs, North Carolina State University, Raleigh, NC, USA

To cite this Article Travis, Karl P. and Gubbins, Keith E.(2001) 'Computer Simulation of Isothermal Mass Transport in Graphite Slit Pores', Molecular Simulation, 27: 5, 405 — 439
To link to this Article: DOI: 10.1080/08927020108031361
URL: http://dx.doi.org/10.1080/08927020108031361

Molecular Simulation, Vol. 27, pp. 405–439
Reprints available directly from the publisher
Photocopying permitted by license only

COMPUTER SIMULATION OF ISOTHERMAL MASS TRANSPORT IN GRAPHITE SLIT PORES

KARL P. TRAVIS[a,*] and KEITH E. GUBBINS[b]

[a]*Department of Chemical and Forensic Sciences, University of Bradford, Bradford BD7 1DP, UK;* [b]*Department of Chemical Engineering, Riddick Labs, North Carolina State University, Raleigh, NC 27695-7905, USA*

(Received June 2001; In final form July 2001)

Results are presented from a simulation study of the mass transport of oxygen and nitrogen through graphite slit pores. The work is motivated by an attempt to understand the molecular origins of the kinetic selectivity displayed when air is separated into its major components using pressure swing adsorption. A combination of non-equilibrium molecular dynamics (NEMD), equilibrium molecular dynamics (EMD) and grand canonical Monte Carlo methods has been employed in our study to extract the maximum information. Transport diffusivities, self-diffusivities, permeabilities and Darken thermodynamic factors have been calculated as a function of pore width and temperature for pure component oxygen and nitrogen. In addition, new EMD simulation data for an 80:20 mixture of nitrogen and oxygen is reported, including a direct calculation of the Stefan–Maxwell coefficients. The results are discussed in terms of the oxygen selectivity and the possible mechanisms, which increase or decrease this quantity.

We find that the pore width behaviour of the diffusion coefficients consists of three distinct regimes: a regime at larger pore widths in which single component diffusion coefficients are largely independent of pore width, an optimum pore width at which both diffusivities increase substantially but the slit pore is selective towards nitrogen, and a regime at very low pore widths at which the diffusivities decrease sharply, but the slits are selective towards oxygen. The mechanism behind each of these regimes is discussed in terms of "entropic" effects and potential barrier heights.

We have also found that permeability selectivity is substantially reduced in a mixture of the two gases with a composition similar to that of air. Cross diffusion coefficients in the mixture have been calculated and shown to be non-negligible.

Keywords: Transport diffusion; Non-equilibrium molecular dynamics; Air separation; Stefan–Maxwell coefficients; Micropores; Adsorption

INTRODUCTION

Porous materials are used extensively in the petroleum and chemical process industries as catalysts and adsorbents. Of the various contributions to the flow of

*Corresponding author.

fluid through these materials, diffusion is the most important, since more often than not, it is the rate determining process. To facilitate the design of improved catalytic and adsorption processes, a greater understanding of the complexities of diffusional behaviour, particularly at the molecular level, are required. Computer simulation is ideally suited to this goal, providing a direct link between the microscopic properties of molecules and macroscopic properties, which are measured in the laboratory.

The motivation behind our current study stems from the important industrial process by which air is separated into its major components by pressure swing adsorption (PSA). In this diffusion-controlled process, a stream of air is passed through a bed of molecular sieving carbon, an adsorbent containing micropores with a mean width of 0.5 nm.

Oxygen selectivities of between 3 and 30 have been reported, even though the kinetic diameters of oxygen and nitrogen differ by less than 0.03 nm. A precise explanation for these large selectivity values remains elusive, despite considerable research. It is important to be able to identify the key parameters in this diffusion process, and then to find their optimum values in order to maximise the amount of oxygen recovered while maintaining economic viability. Several parameters can influence the transport rates of fluids through adsorbents such as molecular sieving carbon; temperature, pore size, and pore morphology, being just a few examples.

The effect of pore width on oxygen selectivity can be probed by experimental methods. Chihara and Suzuki [1] attempted to vary the ratio of diffusivities of oxygen and nitrogen in molecular sieving carbon by adsorption of hydrocarbons followed by heat treatment. They concluded that the absolute diffusivities of oxygen and nitrogen could be decreased by an order of magnitude. However, changing the mean pore width in the adsorbent cannot vary the ratio of their diffusivities. Computer simulation results appear to contradict the finding of Chihara and Suzuki; Seaton *et al.* [2] studied the separation of oxygen and nitrogen in model graphitic pores. They conducted molecular dynamics simulations of self-diffusion in individual pores, and found that the diffusivities were strongly dependent on the pore width. Using a randomly etched graphite pore model (REGP) they found that the degree of kinetic separation observed experimentally could be reproduced at the level of individual pores. In a more recent publication MacElroy *et al.* [3] looked at transport diffusion of oxygen and nitrogen in the same model pore system, concluding that pore length was a controlling factor in the separation mechanism. Recently, Travis and Gubbins [4] investigated the role of pore width on transport diffusion of oxygen and nitrogen mixtures flowing through a single slit using non-equilibrium molecular dynamics (NEMD) techniques.

No significant differences were found between the component diffusivities, except at the lowest pore width studied (0.8375 nm). At this pore width, nitrogen diffuses faster than oxygen, in contradistinction to the experimental observation.

The model used by Travis and Gubbins contained several approximations, for example, the graphitic adsorbent was modelled as a single, smooth walled slit pore, with no account taken of surface structure or electrostatic effects. However, lack of surface structure and electrostatic effects in the model are thought not to be important at ambient temperatures. Furthermore, the use of a single slit pore model of the adsorbent both aids data analysis and provides results, which can be used as input in network models. A key difficulty encountered in our earlier study was the interpretation of the mixture transport coefficients. In this paper, we address this problem by including simulation results for pure component diffusion at similar conditions to the mixture. We also employ equilibrium molecular dynamics (EMD) and grand canonical Monte Carlo (GCMC) simulations to examine how the various contributions to the diffusion coefficients vary with pore width and temperature.

We have organised the paper as follows: in Section 2, we discuss the transport equations for single micropores. In Section 3, we discuss the computer simulation algorithms including the technique of Dual Control Volume Grand Canonical Molecular Dynamics (DCV GCMD), which we have used to obtain most of our diffusion data. In Section 4, we discuss the model and simulation details, and in Section 5, we present and discuss our results. Finally, in Section 6 we present our conclusions.

TRANSPORT IN SINGLE MICROPORES

The starting point for discussing transport in porous membranes is the Dusty Gas model developed by Mason and co-workers [5,6]. The main assumption in this model is that the solid particles, which comprise the membrane, can be treated as if they were a component in the diffusing mixture. This is justified on the grounds that if the adsorbate gas is at low density, a representative volume element must be large enough to contain several molecular mean free paths in order for the postulate of local thermodynamic equilibrium to hold within the volume element. In this case the volume element will contain some of the membrane particles (the "dust"). A single pure gas flowing through a membrane therefore becomes a binary system. A direct manifestation of this treatment is the presence of both viscous and diffusive terms in the flux expressions describing fluid transport through a

membrane. In extreme cases, one of these transport modes will dominate the other. A description of the transport process will then be a furnished by either Fick's law of diffusion, or Poiseuille's law. In membranes with very wide pores, viscous flow can be expected to dominate, while in very narrow pores, diffusion should dominate.

The equations describing the isothermal transport of a multi-component fluid mixture through a membrane can be given either in the Stefan–Maxwell form [7] or, equivalently, in linear irreversible thermodynamic form. The former are the most useful from an engineering point of view, while the latter are more useful in computer simulation studies since the kinetic transport coefficients can be directly related to equilibrium time correlation functions.

The Stefan–Maxwell equations for multi-component fluid flow in a membrane with slit pore geometry (and assuming no viscous separation) are

$$\frac{-1}{k_B T}\left(\frac{\partial \mu_n}{\partial x}\right) = \sum_{m=1}^{K} \frac{\rho_m}{\rho D_{nm}}(u_{nx} - u_{mx}) + \frac{u_{nx}}{D_{n\mathrm{M}}} + \frac{B_0}{\eta D_{n\mathrm{M}}}\left(\frac{\partial p}{\partial x}\right) \tag{1}$$

where μ_n is the chemical potential of fluid species n, T the temperature, ρ the mean fluid density, ρ_m the density of fluid species m, u_n the stream velocity of fluid species n, B_0 is a constant characteristic of the membrane geometry, η is the shear viscosity, p the hydrostatic pressure, while D_{nm} is the Stefan–Maxwell coefficient representing the interdiffision of fluid species n and m. $D_{n\mathrm{M}}$ is the Stefan–Maxwell coefficient representing the diffusion of fluid species n in the membrane denoted by the subscript M.

The linear irreversible thermodynamic expression for the component flux is

$$J_{mx} = -\sum_n L_{mn}\left(\frac{\partial \mu_n}{\partial x}\right) - L_0\left(\frac{\partial p}{\partial x}\right) \tag{2}$$

where J_{mx} is the flux of component m in the x-Cartesian direction of a laboratory frame of reference, L_{mn} are the phenomenological transport coefficients and L_0 is a viscous transport coefficient. The phenomenological coefficients, L_{mn}, are related to microscopic properties of the fluid through Green-Kubo type formulae or their equivalent Einstein mean square displacement formulae

$$L_{mn} = \frac{N_m N_n}{2VK_B T}\int_0^\infty \langle u_m(t) u_n(0)\rangle \mathrm{d}t \tag{3}$$

$$L_{mn} = \frac{N_m N_n}{4VK_B T}\lim_{t\to\infty}\frac{\mathrm{d}}{\mathrm{d}t}\langle [R_m(t) - R_m(0)][R_n(t) - R_n(0)]\rangle \tag{4}$$

where R_m is the centre-of-mass of fluid component m and N_m is the number of molecules of type m. In the special case of single component fluid transport, these equations become, respectively,

$$L_f = \frac{N^2}{2VK_BT}\int_0^\infty \langle u(t)u(0)\rangle \mathrm{d}t \tag{5}$$

$$L_f = \frac{N^2}{4Vk_BT}\lim_{t\to\infty}\frac{\mathrm{d}}{\mathrm{d}t}\langle [R(t) - R(0)]^2\rangle \tag{6}$$

where L_f is the single component transport coefficient.

In the single component case, a simple one to one mapping exists between the phenomenological coefficient L_f and a Stefan–Maxwell diffusion coefficient, $D_{0M}(\equiv D_0)$ which is the limiting case of $D_{n\mathrm{M}}$. This follows from substituting the flux expression ($J = \rho u$) into Eq. (1), rearranging, and then comparing with Eq. (2) to give

$$D_0 = \frac{k_BT}{\rho}L_f \tag{7}$$

We shall henceforth refer to D_0 as the collective diffusivity. The situation for mixtures is more complicated. Only in the case of a binary fluid mixture can tractable relations be derived. The mapping is then

$$\frac{D_{1M}}{k_BT} = \frac{L_{11}L_{22} - L_X^2}{\rho_1 L_{22} - \rho_2 L_X} \tag{8}$$

$$\frac{D_X}{k_BT} = \frac{L_{11}L_{22} - L_X^2}{(e_1 + e_2)L_X} \tag{9}$$

where L_X and D_X represent the cross terms L_{12} and D_{12}, which are identical to L_{21} and D_{21} by symmetry. The equation for D_{22} can be obtained by interchanging the indices in Eq. (8). The inverse relationships can also be written down. These are

$$k_BTL_{11} = \frac{(\rho D_{12} + \rho_1 D_{2M})\rho_1 D_{1M}}{\rho D_{12} + \rho_1 D_{2M} + \rho_2 D_{1M}} \tag{10}$$

$$k_BTL_x = \frac{(\rho_1\rho_2 D_{1M}D_{2M})}{\rho D_{12} + \rho_1 D_{2M} + \rho_2 D_{1M}} \tag{11}$$

with the equation for L_{22} being obtained by interchanging indices in Eq. (10).

The total intrapore flux for a single component fluid flowing through a single slit pore becomes (using Eqs. (2) and (7) and $L_0 = \rho B_0/\eta$),

$$J_x = -\frac{\rho D_0}{k_B T}\left(\frac{\partial \mu}{\partial x}\right) - \frac{\rho B_0}{\eta}\left(\frac{\partial p}{\partial x}\right) \tag{12}$$

where B_0 is a geometric factor characteristic of a slit pore geometry and η is the coefficient of shear viscosity. The first term on the right hand side of Eq. (12) is readily identified as the diffusive contribution to the flux, J_x^{D}, while the other term is the viscous contribution to the flux, J_x^{V}. The expression for the total intrapore flux is then, formally,

$$J_x^{\mathrm{tot}} = J_x^{\mathrm{D}} + J_x^{\mathrm{V}} \tag{13}$$

Using the Gibbs–Duhem equation, the chemical potential gradient appearing in the expression for the diffusive flux can be transformed into a density gradient with the result that

$$J_x^{\mathrm{D}} = -D_0\left(\frac{\mathrm{d}\ln f}{\mathrm{d}\ln \rho}\right)\left(\frac{\partial \rho}{\partial x}\right) \tag{14}$$

where f is the fugacity of the external gas phase that is in equilibrium with the adsorbate. The equation is now in the more familiar Fickian form. The first quantity in parentheses is a thermodynamic factor which is known as the Darken factor. In words, it is the inverse slope of the adsorption isotherm in logarithmic coordinates. The product of D_0 with the Darken factor, is referred to as the transport diffusivity, D_t,

$$D_t = D_0\left(\frac{\mathrm{d}\ln f}{\mathrm{d}\ln \rho}\right) \tag{15}$$

which is the constant of proportionality between the diffusive flux and the density gradient. The form of Eq. (15) shows why D_0 is sometimes referred to as the corrected diffusivity; it has to he corrected for the thermodynamic factor [8]. The transport diffusivity can be expected to have a stronger concentration dependence than the collective diffusivity, D_0, as a result of the concentration dependence of the Darken factor. The Darken factor approaches unity in the limit of vanishing density.

The collective diffusivity, D_0, can be shown to consist of a self diffusivity, D_S, and a diffusivity which arises through momentum cross coupling, D_ξ [9]

$$D_0 = D_s + D_\xi \tag{16}$$

In the limit of zero loading, the cross coupling diffusivity will vanish and D_0 becomes equal to the self diffusivity, D_S, a single particle property.

The pressure gradient appearing in the expression for the viscous flux can be re-written as a density gradient with the effect that an effective transport diffusivity, D_t^{eff}, may be defined as

$$J_x^{\text{tot}} = -D_t^{\text{eff}} \left(\frac{\partial \rho}{\partial x} \right) \tag{17}$$

where the effective diffusivity now contains a viscous contribution. The significance of Eq. (17) will be explained in the next section.

CALCULATION OF TRANSPORT PROPERTIES VIA COMPUTER SIMULATION

In principle, all the transport coefficients appearing in Eq. (2) could be calculated in a single EMD simulation and used to calculate values of the Stefan–Maxwell diffusion coefficients. Once these quantities are known, together with the shear viscosity, the intrapore fluxes may be predicted for a range of different driving forces. However, in practice, the integrals in Eqs. (3) and (5) are notoriously difficult to calculate because the time correlation functions exhibit long time tails and suffer from a poor signal to noise ratio. Recently, a new NEMD method was developed [10–12] which allows the direct simulation of mass transport through membranes under the influence of a chemical potential gradient. This method has been named Dual Control Volume Grand Canonical Molecular Dynamics (DCV GCMD). This type of simulation gives directly the total intrapore fluxes and, as an added bonus, can yield the diffusion coefficients with superior signal to noise compared to the EMD route. With the introduction of more accurate models for membranes and improved intermolecular potentials, DCV GCMD can be expected to be a powerful tool in predicting membrane separation performance.

In the DCV GCMD technique, a gradient in chemical potential is established by placing two particle reservoirs at either end of a single pore and maintaining them at fixed, but different, chemical potentials. This is achieved by periodically conducting a series of creations and deletions according to the prescription of grand canonical Monte Carlo (GCMC). Examples of the uses of DCV GCMD include: a study of the transport diffusion of methane in graphite [12], diffusion of gases in zeolite frameworks [13] diffusion through polymer

membranes [14] and diffusion of a mixture of oxygen and nitrogen through a graphite slit-pore [3,4,15].

The main drawback of DCV GCMD is the difficulty in extracting the diffusion coefficients in an unambiguous manner. Consider the case of a single component fluid in a slit-pore as an example. DCV GCMD gives the total flux directly. However, the total flux in general consists of a diffusive term and a viscous term (Eq. (13)) and the diffusion coefficient obtained from taking the ratio of the total flux to the chemical potential gradient is only an effective diffusion coefficient. There is no simple way to uncouple the two contributions to the total flux. One solution, which has been tried, is to assume the viscous flux is given by the solution of a Poiseuille flow problem [16]. However, such a method is doomed to failure because the quadratic velocity profile predicted by classical hydrodynamics is not observed in pores of less than about 10 molecular diameters in width [17,18] Travis and Gubbins introduced a more fruitful approach [19]. Their solution was to perform the DCV GCMD experiment first and then, knowing the mean density and total flux, perform a second simulation, but this time of pure Poiseuille flow at the same density and equivalent pressure gradient. This relies on the use of a constant force rather than an actual pressure gradient to drive the flow, so that the density profile remains uniform in the flow direction. Since no diffusion occurs, the integrated flux profile yields directly the viscous contribution to the total DCV GCMD flux. The main drawback to this method is that an extra simulation needs to be performed. In some situations the viscous flux is negligible in comparison to the diffusive flux and the problem no longer arises.

One further problem with DCV GCMD is the difficulty in calculating an accurate value of the local chemical potential. It is often more convenient to calculate the local density than the local chemical potential. The result is that the more fundamental transport coefficient, D_0, cannot be obtained directly from a DCV GCMD simulation. To obtain D_0 indirectly from a DCV GCMD simulation, one must perform a series of GCMC simulations, obtain the adsorption isotherm and then calculate the Darken factor from this. In the limit that $\rho \rightarrow 0$, the Darken factor becomes unity and DCV GCMD then gives D_0 directly. However, in this limit, D_0 can be replaced by D_S, the self diffusivity that is more readily obtained by EMD.

The same arguments apply when fluid mixtures are considered: viscous terms. Darken factors, and now, cross coefficients mean that obtaining the Stefan–Maxwell coefficients directly from a DCV GCMD simulation is an arduous task. In order to fully understand the mechanism of diffusion controlled separation processes it is therefore necessary to use a simulation "toolkit" containing in

addition to DCV GCMD, EMD, Poiseuille flow NEMD and GCMC methods. In the present work we report simulations employing a range of these techniques. We have chosen to use a simple slit pore representation of the molecular sieving carbon to facilitate interpretation of the data.

SIMULATION DETAILS

Adsorbate and Adsorbent Models

We represent the interaction of the adsorbate molecules with the graphite planes in our model by a smooth 10-4-3 potential due to Steele [20]. This potential is a function of the z-co-ordinate only. Neglecting the corrugations in the xy graphite planes is expected to be a reasonable approximation for this study, but might be a serious omission at lower temperatures. The total potential energy function, which takes into account the interactions of both graphite planes in a slit-pore is

$$\Phi_{ic} = 4\pi\varepsilon_{ic}\sigma_{ic}^2\Delta n_c\left[\frac{1}{5}\left(\frac{\sigma_{ic}}{(H/2-z)}\right)^{10} - \frac{1}{2}\left(\frac{\sigma_{ic}}{(H/2-z)}\right)^{4} - \frac{\sigma_{ic}^4}{6\Delta(H/2-z+0.61\Delta)^3} + \frac{1}{5}\left(\frac{\sigma_{ic}}{(H/2+z)}\right)^{10} - \frac{1}{2}\left(\frac{\sigma_{ic}}{(H/2+z)}\right)^{4} - \frac{\sigma_{ic}^4}{6\Delta(H/2+z+0.61\Delta)^3}\right] \tag{18}$$

where Δ is the inner layer spacing in graphite, which is taken to be 0.335 nm, $n_c = 114\,\text{nm}^{-3}$ is the carbon atom number density in graphite, H is the pore width, defined as the distance between the centres-of-mass of the innermost graphite planes, while ϵ_{ic} and σ_{ic} are the Lennard–Jones parameters appropriate for interactions between a molecular site of species i and a carbon atom.

Oxygen and nitrogen are modelled as two-centre Lennard–Jones molecules with fixed bond lengths. Interactions between sites on different fluid molecules are modelled with a truncated and shifted Lennard–Jones 12–6 potential:

$$\Phi_{ij}(r) = \begin{cases} 4\varepsilon_{ij}\left(\frac{\sigma_{ij}}{r_{ij}}\right)^{12} - \left(\frac{\sigma_{ij}}{r_{ij}}\right)^{6} - \Phi_{ij}(r_c) & r \le r_c \\ 0 & r > r_c \end{cases} \tag{19}$$

In the above equation, r is the scalar interatomic distance between a pair of interacting sites, r_c is the truncation distance, and $\Phi_{ij}(r_c)$ is the value of the

potential energy at the point of truncation. Lennard–Jones potential parameters for nitrogen, oxygen, and carbon were taken from the literature [21] and are given in Table I. Parameters appropriate for interactions between chemically different species, for example, between an oxygen atom and a nitrogen atom, are given by the Lorentz–Berthelot mixing rules: $\sigma_{ij} = 1/2(\sigma_i + \sigma_j)$ and $\varepsilon_{ij} = \sqrt{\varepsilon_i \varepsilon_j}$ The bond lengths of the molecules are 0.1097 nm for nitrogen and 0.1169 nm for oxygen. We truncate the Lennard–Jones potential at $r_c = 2.5\sigma_{ij}$ (we do not truncate or shift the Steele 10-4-3 potential). We consider only classical dynamics in constructing our model, quantum effects being unimportant for a system such as ours [22]. No account is taken of the quadrupole for nitrogen molecules. Justification for this approximation comes from simulation studies of nitrogen adsorption in slit pores at ambient temperature, which found that the quadrupole had no significant effect on the results [23].

Dual Control Volume Simulations

The DCV GCMD algorithm for use with multi-component mixtures has been discussed in detail elsewhere [4] so we give only a brief description of its implementation here.

There are several variations of DCV GCMD but essentially the algorithm consists of performing numerous cycles, each of which comprises a molecular dynamics step, in which the trajectories of all fluid molecules are incremented, followed by a series of Grand Canonical Monte Carlo creations and destructions of either species in each of the two control volumes.

A creation attempt of a molecule of species γ in control volume c is accepted with a probability,

$$\min[1, \exp[-\beta \Delta v_\gamma + \ln(z_\gamma(c)V(c)/(N_\gamma + 1))]] \tag{20}$$

where $V(c)$, N and $z(c)$ are the volume, the current number of molecules in control volume c and the activity in control volume c, respectively, while Δv is the energy change accompanying the insertion of a molecule into the control volume, and $\beta = 1/k_B T$.

TABLE I Lennard–Jones potential parameters for oxyzen, nitrogen and carbon used in this work

Atom	σ (nm)	k_B^{-1} (ε/K)
Carbon	0.340	28.0
Nitrogen	0.3296	60.39
Oxygen	0.2940	75.49

Destructions of molecules are accepted with a probality

$$\min[1, \exp[-\beta \Delta v_\gamma + \ln(N_\gamma/(z_\gamma(c)V(c)))]] \tag{21}$$

where Δv is now the energy change accompanying the destruction of a molecule from control volume c.

When molecules are created in either control volume, they are assigned thermal components of both translational velocity and angular velocity selected from a Maxwell–Boltzmann distribution. Furthermore, newly created molecules are given an appropriate initial component of streaming velocity to ensure creations are compatible with mass transport (further details are given below).

Control volumes are placed at each end of the slit-pore. Placing the control volumes inside the pore eliminates pore-entrance effects and greatly simplifies the interpretation of our results. We define our co-ordinate system such that the flow is the x-direction and the graphite planes are separated along the z-direction. The volume of the control volumes is taken to be the same as that of the flow region in between them (see Fig. 1). We note that there is no unambiguous definition of volume in a porous membrane. However for simplicity, we define the volume of the flow region and control volumes to be $V = HL_xL_y$, which contains a certain amount of dead space due to the implicit carbon atoms in graphite. The control volumes and the flow region have a length in the x-direction of $L_x = 9.888$ nm, while in the y-direction, $L_y = 9.888$ nm. The total number of molecules in the simulation cell varied between 1200 and 3600 molecules.

The system is kept isothermal via the following scheme: The simulation box is divided into 21 bins of equal volume along the flow direction. The local temperature in each bin is then controlled by means of the Nosé–Hoover thermostat [24,25]. In a molecular dynamics step, a fifth order Gear algorithm [26] was used to integrate Hamilton's equations of motion, supplemented with a

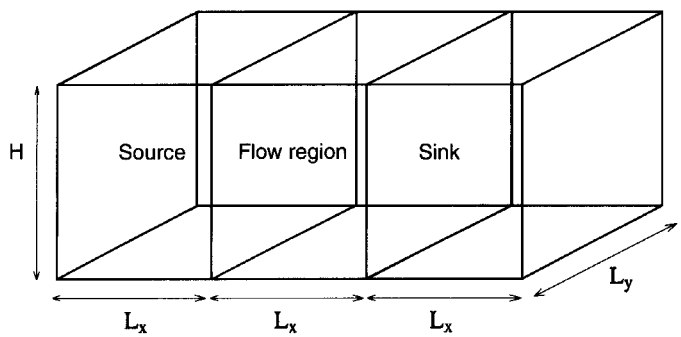

FIGURE 1 Schematic diagram of the simulation cell for DCV GCMD. Flow takes place in the x-direction from the source to the sink control volume.

Nosé–Hoover thermostatting scheme [24,25], and Gaussian constraints [27,28] to fix the diatomic bond lengths. The integration time step was chosen to be 2.5 fs. Periodic boundary conditions operate in the y-direction. There are no periodic boundary conditions in the x-direction; the ends of the simulation box are dissolving boundaries. That is, if a molecule reaches either of these boundaries it is removed from the simulation

To ensure that molecular creations are compatible with mass transport, a component of streaming velocity is added to the thermal velocity of newly created molecules. We determine this component of streaming velocity by taking a value for the flux at the centre of the flow region and dividing this by the concentration in the appropriate control volume. Since we begin the simulation with zero molecules, initially there will be no measurable flux. As molecules begin to diffuse through the pore, a steady state flux will gradually develop, which is constant at any yz plane in the simulation cell. To prevent the streaming velocity from diverging, we follow Cracknell *et al.* [12] and introduce a degree of course graining. The method of augmenting the molecular velocities upon creation proceeds as follows: we allow a settling time of 50000 steps for obtaining sufficient molecules in the flow region to obtain a flux. After this time, we divide the flux (averaged over the settling time) by the average concentration in the control volume of interest. This streaming velocity is then added to the thermal component of velocity of newly created molecules in that control volume. After the settling time, the flux is averaged over periods of 1000 molecular dynamics steps and used in the subsequent calculations of the streaming velocity in the control volumes.

Because we employ a smooth potential to represent the graphite planes in a real carbon pore, we need to account for the exchange of momentum that would take place between fluid molecules and the carbon atoms in a real adsorbent. We employ the so-called diffuse boundary condition, based on the diffuse boundary conditions used by Cracknell *et al.* [12] but modified here for the case of molecules. Application of our molecular diffuse boundary condition proceeds as follows: After each molecular dynamics time step we check to see if the following two conditions are satisfied:

(1) The centre-of-mass momentum (in the laboratory frame) of a given molecule in the z-direction has reversed in sign;
(2) The centre-of-mass of that same molecule is within the repulsive region of the Steele 10-4-3 potential.

If, and only if, both of these conditions are satisfied, we reselect the centre-of-mass momentum of that molecule in the directions parallel to the confining surface from a Maxwell–Boltzmann distribution at the appropriate temperature.

One important control parameter in DCV GCMD is the ratio of stochastic to dynamic steps, n_{MC}/n_{MD}. An optimum value for n_{MC}/n_{MD} was arrived at by finding the smallest value, which still yielded the correct concentrations of the two species obtained from conducting separate grand canonical adsorption simulations at the relevant thermodynamic state point for the two control volumes. Using too large a value for this parameter greatly increases the CPU time needed to reach a non-equilibrium steady state. We find that for our simulations a value for n_{MC}/n_{MC} of 50 is optimum.

For the pure component simulations, we used the same activities as for the mixture simulations [4] i.e. the activity gradients of pure oxygen and pure nitrogen were identical to the appropriate activity gradients in the mixture. The set of activities appropriate to the two temperatures studied: t=0 and 25°C are given in Table II. Since the fugacities are the same as the partial fugacities in the mixture, and the bulk gases are close to ideal under these conditions, it follows that the pressure of each pure gas is the same as its partial pressure in the mixture.

A series of simulations was carried out at the following set of pore widths: $H/\Delta = \{5.0, 4.0, 3.0, 2.5, 2.0, 1.9\}$, where Δ is the graphite layer spacing. The length of these simulations ranged from a minimum of 12 million molecular dynamics steps at the highest pore width to about 36 million steps for the lowest pore width.

EMD Simulations

Equilibrium molecular dynamics simulations were performed for the purpose of calculating the phenomenological transport coefficients, L_{mn} and L_f, plus the coefficient of self-diffusion. The algorithm for the EMD simulations was similar to that used in the dynamic portion of the DCV GCMD simulations with the exception that the overall temperature was thermostatted rather than the local temperature in bins. The diffuse scattering algorithm was also applied in these simulations. A system size consisting of 1000 molecules in total was used throughout. The mean square displacements appearing in Eqs. (4) and (6) were calculated along with the molecular mean square displacements over a 100 ps

TABLE II Activities used in the DCV GCMD mixture and pure component simulations

Species	$t = 0$ (°C)		$t = 25$ (°C)	
	Z_{source} (nm^{-3})	Z_{sink} (nm^{-3})	Z_{source} (nm^{-3})	Z_{sink} (nm^{-3})
Nitrogen	0.3116	0.2083	0.2867	0.1902
Oxygen	0.0780	0.0521	0.0717	0.0479

time frame. Single component EMD simulations were performed at the same set of pore widths and mean densities as used/determined in the DCV GCMD simulations. Mixture simulations were performed at the single pore width of 2.5Δ but at the mean densities and compositions taken from the source and sink control volumes in the mixture DCV GCMD simulations reported in a previous publication [4]. Starting configurations at the appropriate density were obtained by using GCMC to place the molecules inside the pore. These configurations were then equilibrated for 500,000 time steps followed by a production run of 5 million steps, except in the case of the mixture simulations, which were run for 20 million production steps in order to obtain reasonable signal to noise on the cross coefficients.

GCMC Simulations

In order to calculate the Darken factors, a series of GCMC simulations were performed in slit-pores having the same range of pore sizes as used in the pure component simulations. In each of these adsorption simulations, the absolute number of molecules within the pore volume was calculated at a range of filling pressures. Each simulation consisted of 30 million attempted Monte Carlo moves (a move can either be a combined rotation-translation, creation or destruction), of which the first 10 million moves were rejected prior to the averaging process. No mixture adsorption simulations were performed.

RESULTS AND DISCUSSION

DCV GCMD Pure Component Simulation

Pure component, effective transport diffusivities were obtained from the DCV GCMD simulations by taking the ratio of the total steady state flux and the gradient of the number density. These diffusivities are plotted as a function of pore width and temperature in Fig. 2. The figure shows that the diffusion coefficient of either species is relatively insensitive to density and temperature at pore widths above 1 nm. The diffusion coefficient of nitrogen is always greater than that of oxygen in this same regime. In the sub-nanometer range of pore widths, diffusivity coefficients become stronger functions of both density and temperature. At a pore width of 0.8375 nm the diffusion coefficients of both oxygen and nitrogen substantially increase, the size of this increase being more marked for the latter species. Lowering the temperature results in a greater increase in diffusivity in both cases. As the pore width is reduced below

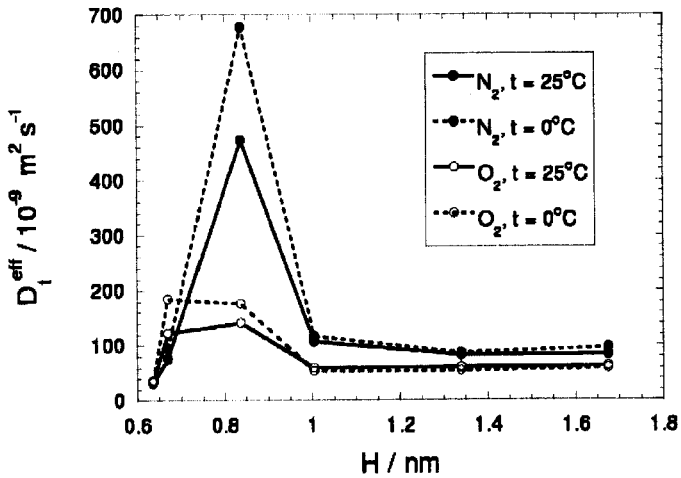

FIGURE 2 Plot of effective transport diffusivity against pore width for nitrogen (solid lines) and oxygen (dashed lines), at $t = 0$°C (open circles), and $t = 25$°C (filled circles). Data obtained from pure component DCV GCMD simulations.

0.8375 nm, the diffusion coefficient of nitrogen decreases sharply while that of oxygen decreases a little at 25°C and rises slightly at 0°C before falling again at the lowest pore width. Over a narrow range of pore widths in the sub-nanometer range, the diffusive selectivity changes from a value favouring nitrogen to one favouring oxygen. To understand these differences it is necessary to examine the various contributions to the effective transport diffusivity such as the thermodynamic factors. Equilibrium simulations were performed to enable such an analysis to be made. It should be pointed out that the DCV GCMD simulations are still essential for obtaining the total intrapore fluxes since these are needed for the calculation of permeabilities.

EMD Pure Component Simulations

Equilibrium molecular dynamics simulations were conducted for pure oxygen and pure nitrogen as detailed in "Calculation of transport properties via computer simulation". Mean square displacements of the centre-of-mass position of the entire fluid and of individual molecules were averaged over the course of these simulations in order to calculate the appropriate diffusion coefficients defined by Eqs. (4) and (6).

The self diffusivities are plotted as a function of pore width and temperature in Fig. 3. From the figure it can be seen that self-diffusivity increases with increasing pore width and temperature for both components. Furthermore,

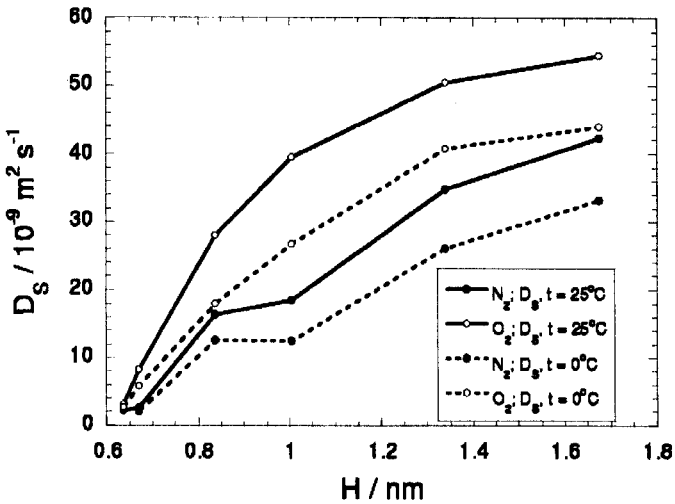

FIGURE 3 Plot of self diffusivity against pore width for nitrogen (filled circles) and oxygen (open circles) at $t = 0°C$ (dashed lines) and $t = 25°C$ (solid lines). Data obtained from pure component EMD simulations.

oxygen self-diffusivity is always greater than nitrogen self-diffusivity. These results are in line with the behaviour of D_S in the bulk phase; lowering the pore width corresponds to increasing the density and hence lowering of the molecular mobility. Lower temperatures also lead to lower mobility, and hence, lower D_S values. The nitrogen self-diffusivity plots have a small anomaly at $H = 1.005$ nm. Here the self-diffusivity is lower than expected. This can be explained in terms of density. Figure 4 shows the density as a function of pore width and temperature. At a pore width of 1.005 nm, the nitrogen density is higher than expected, the effect being stronger at the lower temperature. This feature is absent from the corresponding oxygen density plots. The anomalous nitrogen density at $H = 1.005$ nm is presumably a molecular packing effect.

The collective diffusion coefficient, D_0, is notoriously difficult to obtain with reasonable signal-to-noise. To illustrate this fact, mean square displacements of the fluid centre-of-mass are plotted as a function of pore width for nitrogen at 25°C in Fig. 5. Except at the narrowest pore widths, the mean square displacement curves are quite noisy despite the use of long simulation times. Figure 6 shows a plot of the collective diffusivity. D_0, against pore width for oxygen and nitrogen.

It is clear that the collective diffusion coefficient has a more complicated dependence on pore width and temperature than the self diffusion coefficient. At 0°C, D_0 is lower for oxygen than at 25°C. This result stands in contrast to the temperature behaviour of the effective transport diffusivity in Fig. 2. In the case

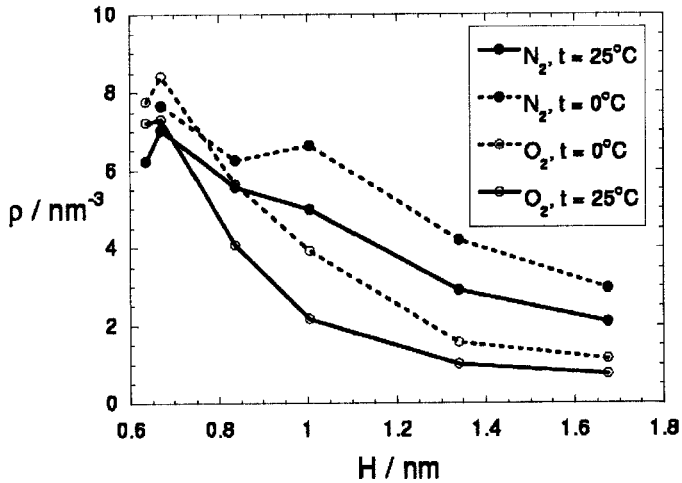

FIGURE 4 Plot of absolute number density against pore width for nitrogen (filled circles) and oxygen (open circles) at $t = 0$°C (dashed lines) and $t = 25$°C (solid lines). Densities are those obtained from pure component DCV GCMD simulations.

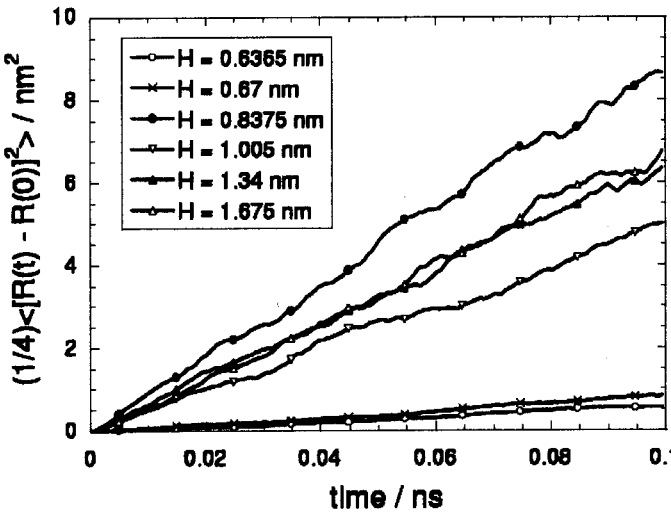

FIGURE 5 Centre-of-mass mean square displacements plotted as a function of time for nitrogen at $t = 25$°C and various pore widths. Data obtained from pure component EMD simulations.

of nitrogen, at some pore widths D_0 is lower at the lower temperature while at others, it is higher at lower temperature. Again, this stands in sharp contrast to the behaviour shown in Fig. 2. A possible explanation for these differences is the pore width and temperature dependence of the thermodynamic factor (Darken factor). We turn our attention to this in the next section.

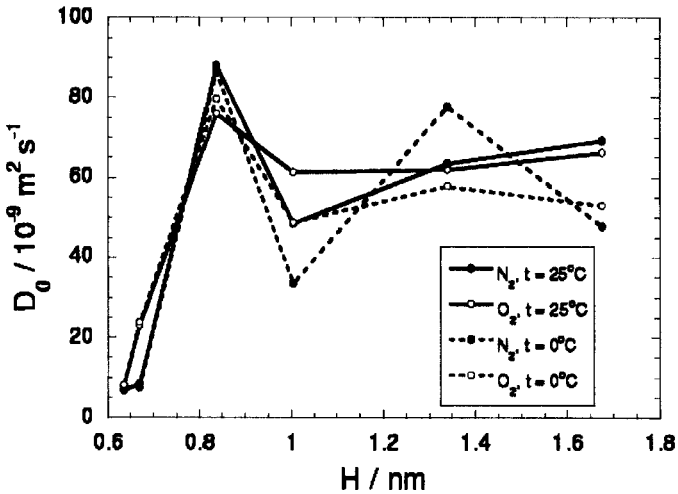

FIGURE 6 Plot of collective diffusivity. D_0, against pore width for nitrogen (filled circles) and oxygen (open circles) at $t = 0$°C (dashed lines) and $t = 25$°C (solid lines). Data obtained from pure component EMD simulations.

Figure 6 shows that all the diffusivity curves display a maximum at a pore width of 0.8375 nm in common with the behaviour of the effective transport diffusivity. The collective diffusivity of nitrogen at this point is greater than that of oxygen but this difference is clearly much smaller than seen in the case of D_t^{eff}. Once again we attribute this fact to the thermodynamic factor. At the lower pore width of $H = 0.67$ nm. D_0 for oxygen is greater than that for nitrogen although both diffusivities are substantially lower than they are at 0.8375 nm.

It is of interest to calculate the cross coupling contribution to the collective diffusivity, D_ξ (defined in Eq. (16)). At low loadings, D_ξ is expected to vanish so that the collective and self diffusivities become equal. This fact can be used to calculate transport diffusivities from knowledge of the self-diffusivity and the Darken factor if diffusion occurs at low adsorbate density. However, the densities involved in this work are far removed from the zero loading limit and so the self-diffusivity cannot be expected to equal D_0. Figure 7 shows a plot of D_ξ as a function of pore width and temperature for oxygen and nitrogen. The behaviour of D_ξ at 25°C is remarkably similar to the pore width dependence shown by the effective transport diffusivity: insensitivity to pore width above 1 nm, a steep rise at $H = 0.8375$ nm followed by a drop at lower pore widths. The nitrogen D_ξ is greater than the oxygen D_ξ at pore widths greater than 0.67 nm. The pore width behaviour of the effective transport diffusivity results from the pore width dependence of D_ξ. The temperature dependence of D_ξ is complicated. At some pore widths, a lower temperature results in a lower value of D_ξ while at others, it

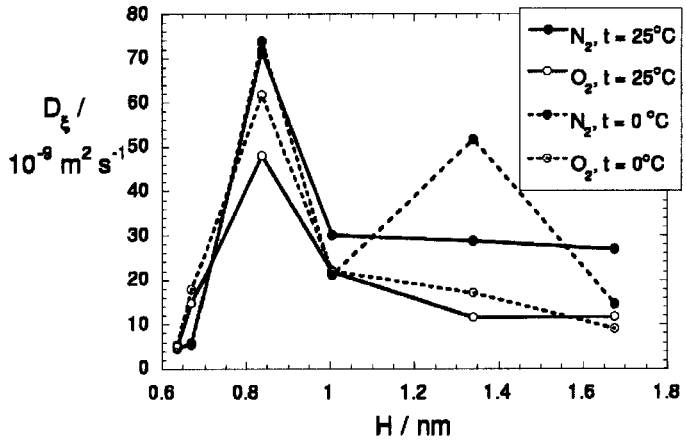

FIGURE 7 Plot of the cross coupling diffusivity, D_ξ against pore width for nitrogen (filled circles) and oxygen (open circles) at $t = 0$°C (dashed lines) and $t = 25$°C (solid lines). Data obtained from pure component EMD simulations.

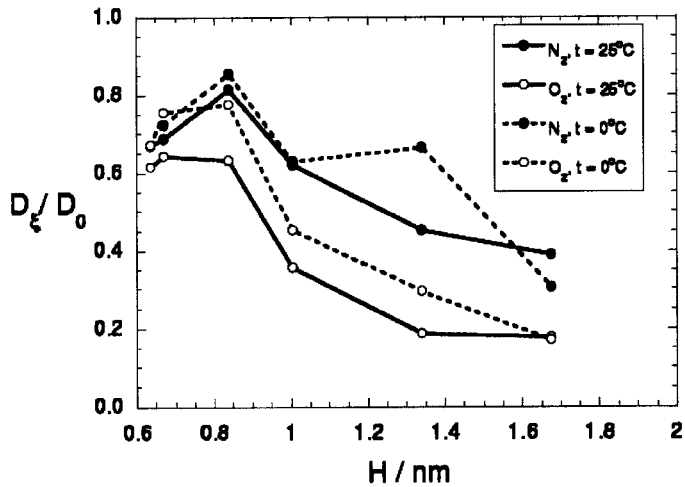

FIGURE 8 Plot of the ratio of the cross coupling diffusivity, D_ξ, to the collective diffusivity. *D0*, against pore width for nitrogen (filled circles) and oxygen (open circles) at $t = 0$°C (dashed lines) and $t = 25$°C (solid lines). Data obtained from pure component EMD simulations.

is increased. In the case of nitrogen at 0°C, the diffusivity has two maxima at pore widths of 1.34 and 0.8375 nm. A useful quantity to calculate is the ratio of D_ξ to D_0, which measures the influence of the momentum cross correlations in determining the collective diffusivity. Figure 8 shows a plot of this ratio against pore width and temperature for oxygen and nitrogen. The figure shows the increasing importance of this cross correlation diffusivity as the pore width is

decreased. Lowering the temperature also increases the contribution from D_ξ relative to the self diffusivity. Comparing Figs. 4 and 8 we see that increasing adsorbate density is chiefly responsible for the growing contribution made by D_ξ to D_0. It is clear from Fig. 8 that the product of the self diffusivity and the Darken factor would seriously underestimate the value of D_0 and as a consequence, miss the important pore width behaviour of the transport diffusivity. The increase in D_ξ/D_0 with decreasing temperature reflects the greater adsorbate density at the lower temperature.

In all the pure component data presented so far, the density varied along with pore width. In order to look at the effects of these two variables separately, we conducted EMD simulations at the lowest two pore widths, with $t = 25°C$, for a range of densities. The results of these simulations are shown in Figs. 9 and 10. In Fig. 9 we see that D_0 for nitrogen is greater than D_0 for oxygen across the entire density range. The oxygen D_0 value is only weakly density dependent whereas that for nitrogen shows two maxima occuring at densities of 3 and 4.5 nm^{-3}. The latter density gives rise to a maximum nitrogen diffusive selectivity. The self-diffusivities show a small selectivity toward oxygen at all densities studied. Turning now to Fig. 10, the D_0 selectivity is now inverted so that oxygen diffuses faster than nitrogen at all densities. Furthermore, the degree of selectivity is much greater than it was at the wider pore width. The oxygen D_0 value increases with

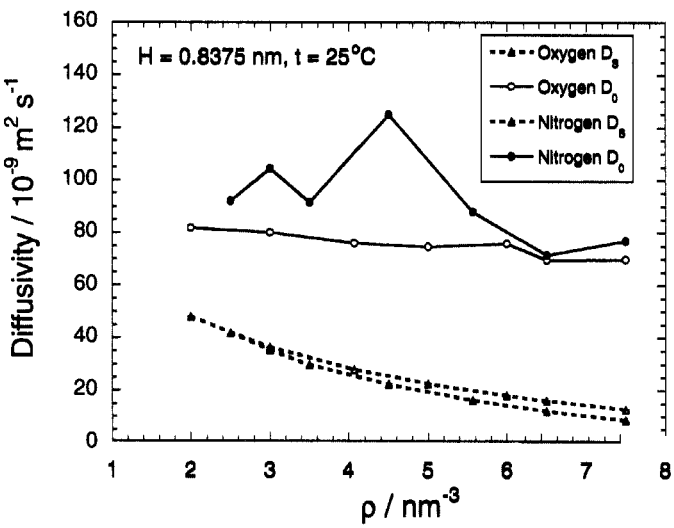

FIGURE 9 Plot of self diffusivity, D_s (dashed lines), and collective diffusivity. D_0 (solid lines), against density at a pore width of $H = 0.8375$ nm ($= 2.5\Delta$) and temperature $t = 25°C$. The different symbols correspond to nitrogen (filled symbols) and oxygen (open symbols). Data obtained from pure component EMD simulations.

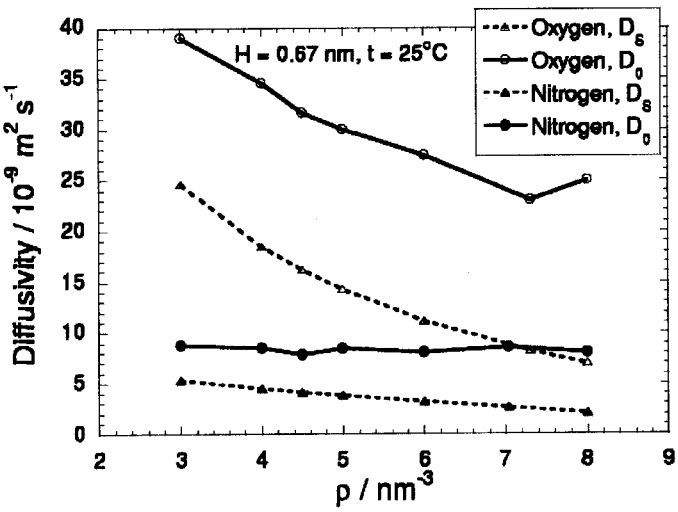

FIGURE 10 Plot of self diffusivity, D_s (dashed lines), and collective diffusivity. D_0 (solid lines), against density at a pore width of $H = 0.67\,\text{nm}(= 2\Delta)$ and temperature $t = 25°\text{C}$. The different symbols correspond to nitrogen (filled symbols) and oxygen (open symbols). Data obtained from pure component EMD simulations.

decreasing density (with the exception of a small increase at the highest density) and does not go through a maximum, while the nitrogen D_0 value is virtually independent of density. At $3\,\text{nm}^{-3}$, the D_0 selectivity is about 4 while the D_S selectivity is around 5. The contrast between the diffusivities and their density dependence in Figs. 9 and 10 suggests different diffusion mechanisms are in operation at the two different pore widths.

GCMC Adsorption Simulations

The difference between the transport diffusivity and the collective diffusivity is a thermodynamic multiplication factor known as the Darken factor (Eq. (15)). Much of the density dependence of D_t is associated with this factor. It is therefore important to know what that density dependence is as a function of pore width. Adsorption isotherms were generated for both pure component fluids at the two temperatures of interest by GCMC. A selection of these isotherms at 25°C is plotted in Fig. 11a. All isotherms are simple type I isotherms. Outside of the Henry law region, at a given filling pressure, we see that oxygen is more strongly adsorbed than nitrogen. As the pore width is reduced, the amount of either species of gas adsorbed increases at the lower pressures. This latter observation is a direct

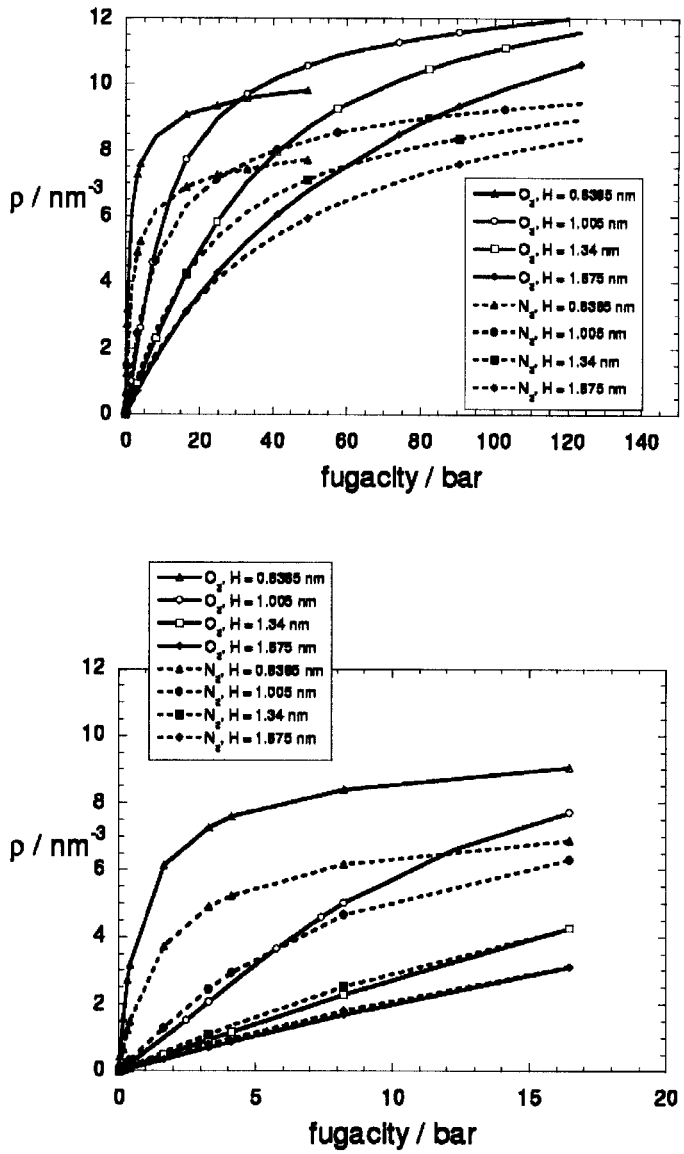

FIGURE 11 (a) Adsorption isotherms plotted at various pore widths for oxygen (solid lines and open symbols) and nitrogen (broken lines and filled symbols) at a temperature, $t = 25°C$. The symbols used in the figure correspond to: $H = 0.6365$ nm (triangles), $H = 1.005$ nm (circles), $H = 1.34$ nm (squares) and $H = 1.675$ nm (diamonds). Data obtained from equilibrium GCMC simulations. (b) As for (a), but showing the 0–20 bar fugacity regime in more detail.

result of the increased overlap of the potential energy surfaces of both graphite planes as they move closer together. Greater overlap results in deeper potential energy wells, which leads to greater adsorption. At high filling pressures, beyond monolayer coverage, entropic effects dominate the adsorption process. The smaller oxygen molecule is more easily accommodated than the slightly bulkier nitrogen molecule. At the low filling pressures used in the DCV GCMD simulations (see Fig. 11b), the differences between nitrogen and oxygen adsorption are less significant. Indeed, apart from the lowest pore widths, nitrogen is more strongly adsorbed than oxygen. At the lowest pore width, entropic effects once again dominate which favours the smaller oxygen molecules. Based on these results, we can speculate that adsorption selectivity in a mixture of the two gases would be small at the operating pressures used in DCV GCMD simulations but would increase in favour of oxygen at high pressures and very low pore widths.

In order to calculate the Darken factors, we fitted our isotherm data to the following equation

$$\ln f = A + \ln \rho + B_1\rho + B_3\rho^3 + B_5\rho^5 \tag{22}$$

where B_1, B_3 and B_5 are empirical parameters. The expression for the Darken factor follows from differentiating Eq. (22) with respect to $ln\,\rho$. This gives

$$\frac{\mathrm{d}\ln f}{\mathrm{d}\ln \rho} = 1 + B_1\rho + 3B_3\rho^3 + 5B_5\rho^5 \tag{23}$$

from which it can be seen that the limiting value of the Darken factor as $\rho(\rightarrow 0$ is unity. Darken factors have been generated for a range of densities at each pore width based upon the values of the coefficients B_1–B_5 obtained in the above fitting procedure. A selection of these factors at 25°C is plotted in Fig. 12 as a function of density. From the figure we see that at any given density, the Darken factor increases as pore width decreases with the exception of the nitrogen factor between pore widths of 1.34 and 1.675 nm where this trend is reversed. At a given pore width, the Darken factor for nitrogen is greater than that of oxygen across a wide range of density. There is one exception to this trend. At the pore width of 1.34 nm, the Darken curves cross over at a density of 11.5 nm^{-3} such that oxygen has the greater Darken factor at higher densities. We cannot attach too much significance to this anomalous behaviour since the Darken factors have been extrapolated to densities higher than those found in the GCMC simulations.

In Fig. 13, various dynamic selectivity measures are plotted against pore width. These selectivity measures are defined as the ratio of an oxygen diffusivity and nitrogen diffusivity or oxygen Darken factor and nitrogen Darken factor. Taking first the collective diffusivity ratio, $D_{0,O_2}/D_{0,N_2}$, we see that this factor indicates a

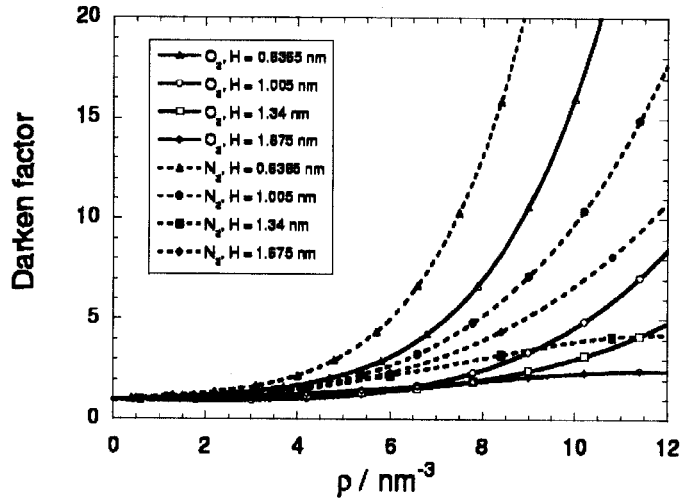

FIGURE 12 Plot of Darken factors ($\mathrm{d}\ln f/\mathrm{d}\ln\rho$), against density for oxygen (solid lines and open symbols) and nitrogen (broken lines and filled symbols), at a temperature, $t = 25°C$. The symbols used in the figure correspond to: $H = 0.6365$ nm (triangles), $H = 1.005$ nm (circles), $H = 1.34$ nm (squares) and $H = 1.675$ nm (diamonds). These curves were generated using Eq. (23).

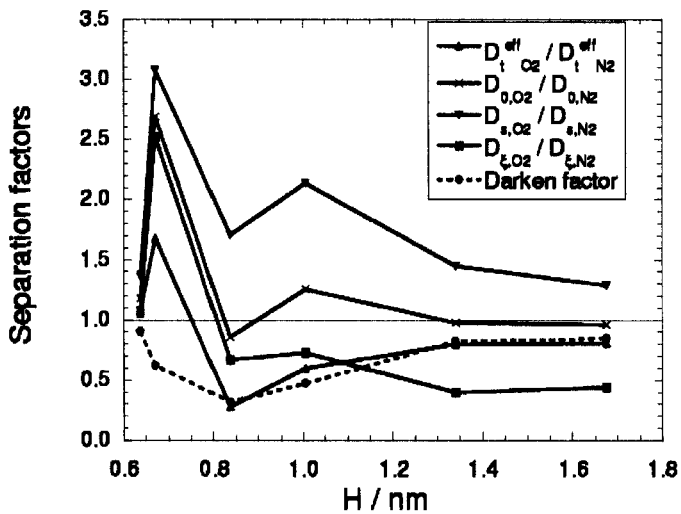

FIGURE 13 Plot of various separation factors (defined as the ratio of an oxygen difffusivity or Darken factor to the nitrogen diffusivity or Darken factor) against pore width at $t = 25°C$.

maximum selectivity for nitrogen at a pore width of 0.8375 nm and a maximum selectivity for oxygen at the lower pore width of 0.67 nm. The Darken factor ratio works in favour of nitrogen at all pore widths although it is a maximum for nitrogen at 0.8375 nm. It is the Darken factor contribution, which strongly

enhances the dynamic selectivity at this pore width, as can be seen by comparing the collective diffusivity ratio, $D_{0,O_2}/D_{0,N_2}$, with the effective transport diffusivity ratio, $D^{\text{eff}}_{t,O_2}/D^{\text{eff}}_{t,N_2}$. The Darken factor works against oxygen at 0.67 nm, lowering the oxygen selectivity from 2.7 to 1.7 in the case of the effective transport diffusivity.

We now address the viscous contribution to the total flux. As detailed elsewhere, the diffusion coefficients obtained from our DCV GCMD simulations are strictly speaking, only *effective* transport diffusivities. To obtain the true transport diffusivity, one can either use the viscous subtraction method [19] to yield the diffusive flux by NEMD, or one can multiply the collective diffusivity by the Darken factor (equilibrium route). The difference between the DCV GCMD effective transport diffusivity and the equilibrium calculated transport diffusivity is a measure of the viscous contribution to the flow. Figure 14 shows a plot of both transport diffusivities as a function of pore width at 25°C. As the figure shows, the difference between the two diffusivities is insignificant. At one or two pore widths, the transport diffusivity of oxygen appears to be greater than the effective transport diffusivity, which is counterintuitive. We believe this simply reflects the statistical uncertainties in the former diffusivity relative to the latter. For pores in the range we have studied it is safe to assume that the viscous contribution to flow is weak in comparison to the diffusive contribution. To a good approximation, the effective transport diffusivity may be used instead of the true transport diffusivity.

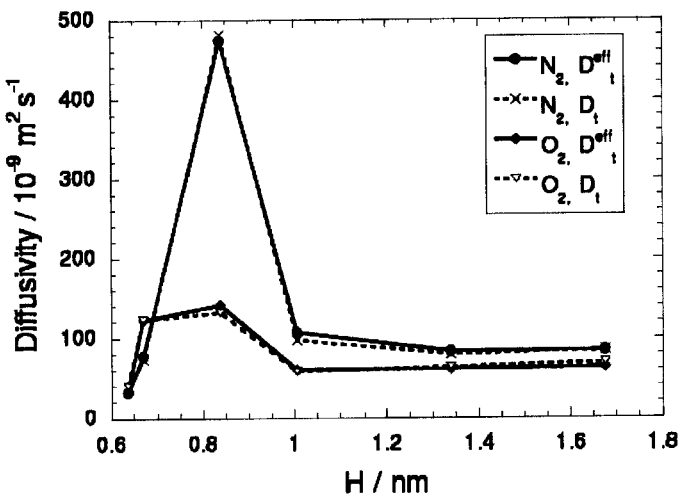

FIGURE 14 Comparison of the effective transport diffusivity (solid lines) obtained via DCV GCMD and the transport diffusion coefficient obtained from the product of the collective diffusivity and the Darken factor (broken lines). Data shown refer to a temperature of $t = 25$°C.

Comparison of Mixture and Pure Component Data

In a previous publication [4] we reported DCV GCMD results for an 80:20 mixture of nitrogen and oxygen diffusing through graphite slits identical to those in our current study. In order to compare diffusion coefficients of either species in the mixture with those of the pure components, we have performed EMD simulations with such an 80:20 mixture at 25°C and a pore width of 0.8375 nm in order to calculate the Stefan–Maxwell coefficients in the mixture. Recall that the DCV GCMD mixture simulations cannot yield these coefficients unambiguously. Because the composition and density in the source and sink control volumes differed in the DCV GCMD mixture simulations [4], separate EMD simulations were performed at these compositions and densities to see what effect this had on the results. The density and composition in the source was: $\rho = 6.044\,\text{nm}^{-3}$, $x_{N2} = 0.18$, while in the sink it was: $\rho = 5.644\,\text{nm}^{-3}$, $x_{N2} = 0.17$. These simulations had to be run for a total of 20 million time steps each so that we had a good signal to noise ratio on the data. Because of the extremely long simulation times, we conducted these runs at a single pore width.

The mean square displacements plotted against time from the higher density simulation are shown in Fig. 15. This figure gives an idea of the accuracy of our data. The mean square displacements are reasonably linear in time. The nitrogen–nitrogen curve shows a much steeper gradient than either the oxygen–oxygen, or the cross coupling curves. The phenomenological coefficients L_{ij}

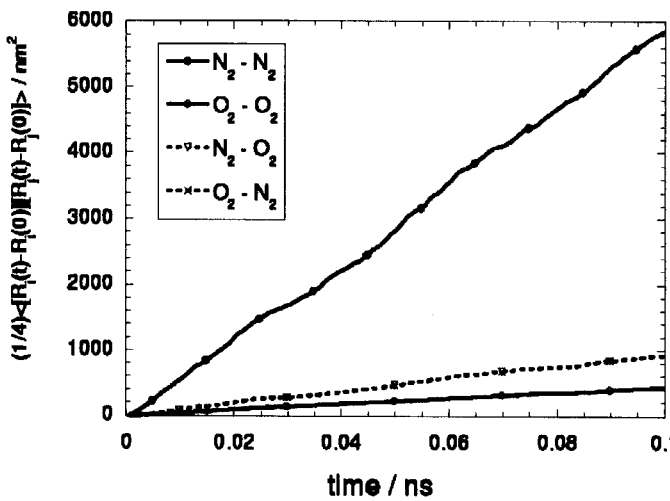

FIGURE 15 Plot of mean square displacements versus time for the 80:20 mixture at $t = 25$°C and $H = 0.8375$ nm. Data obtained from EMD simulations.

TABLE III Phenomenological transport coefficients for the 80:20 mixture of nitrogen and oxygen at $t = 25°C$ obtained using Eq. (4). The quantities in parentheses are the statistical uncertainties in the last digits and represent the error in the slope of the linear portion of the mean square displacement plots. The subscripts 1 and 2 refer to nitrogen and oxygen, respectively

	Source	*Sink*
$k_B V L_{11}$ ($10^{-6}\,m^2\,s^{-1}$)	59.370(93)	55.83(14)
$k_B V L_{12}$ ($10^{-6}\,m^2\,s^{-1}$)	9.342(32)	7.994(23)
$k_B V L_{21}$ ($10^{-6}\,m^2\,s^{-1}$)	9.333(36)	7.982(22)
$k_B V L_{22}$ ($10^{-6}\,m^2\,s^{-1}$)	4.234(7)	4.371(5)

obtained from the slopes of these curves are given in Table III. Here $1 = O_2$, $2 = N_2$. The first thing to note about these quantities is that within the statistical uncertainties, $L_{12} = L_{21}$, in agreement with Onsager's regression hypothesis. Second, L_{11} is an order of magnitude greater than L_{22} while the cross coefficient L_{12} is a little over twice as large as L_{22}. Clearly, the cross diffusion coefficient is significant in magnitude. The L_{ij} coefficients were converted into Stefan Maxwell mutual diffusion coefficients using Eqs. (8) and (9), in which L_x is taken to be the mean value of L_{12} and L_{21}, the results being collected in Table IV. From Table IV we see that D_{1M} is almost twice the magnitude as D_{2M} at the higher density, but only 25% larger at the lower, sink density. In order to compare D_{1M} and D_{2M} with the D_0 values obtained from the pure component simulations at the same temperature and pore width, we first average the values for the source and sink conditions. For the mixture we have $\bar{D}_{1M} = 86 \times 10^{-9}\,m^2\,s^{-1}$, $\bar{D}_{2M} = 59 \times 10^{-9}\,m^2\,s^{-1}$ while for the pure components we have $D_0^{N_2} = 88 \times 10^{-9}\,m^2\,s^{-1}$, $D_0^{O_2} = 76 \times 10^{-9}\,m^2\,s^{-1}$. From this comparison we note that in the case of nitrogen, its diffusion through the slit pore is only marginally effected by the presence of the oxygen component. Oxygen diffusion on the other hand is significantly reduced in the mixture at this pore width and temperature. One important observation from this set of simulations is that L_x(and hence D_x), the cross diffusion coefficient, is non-negligible. This will obviously have important consequences for the total intrapore fluxes. The nitrogen flux is essentially

TABLE IV Stefan–Maxwell coefficients for the 80:20 mixture of nitrogen and oxygen at $t = 25°C$ obtained using Eqs. (8) and (9) with L_{12} and L_{21} symmetrised. The subscripts 1 and 2 refer to nitrogen and oxygen, respectively. The quantities in parentheses are the statistical uncertainties in the last digits

	Source	*Sink*
D_{1M} ($10^{-9}\,m^2\,s^{-1}$)	91.667	79.392
D_{2M} ($10^{-9}\,m^2\,s^{-1}$)	54.184	63.001
D_x ($10^{-9}\,m^2\,s^{-1}$)	17.581	22.564

determined by the L_{11}, coefficient while the oxygen flux is determined by contributions from both L_{22} and L_x. We note that MacElroy and Boyle observed that the diffusion cross coupling for methane–hydrogen mixtures was weak [29].

The performance of a membrane in separating gas mixtures is frequently discussed in terms of the permeability of a given gas species. The permeability, F, which is the pressure and thickness normalised flux, is defined by

$$F_i = \frac{J_i}{(\Delta p_i / L)} \tag{24}$$

where, J_i is the molecular flux of component i and Δp is the pressure drop across a membrane of length L. In the mixture simulations, the partial pressure drops of nitrogen and oxygen were 4 bar and 1 bar, respectively. The pure component pressure drops were chosen to be the same as these mixture partial pressure drops.

A selectivity measure based on the species permeabilities, the so-called permselectivity, is defined by

$$\alpha_{O_2/N_2} = \frac{F_{O_2}}{F_{N_2}} \tag{25}$$

Permselectivity values are plotted in Fig. 16 for both pure component data and mixture data as a function of pore width. The main feature of Fig. 16 is the large difference between the pure component and mixture selectivities. In the mixture case, oxygen selectivity varies weakly with pore width, reaching a value of about

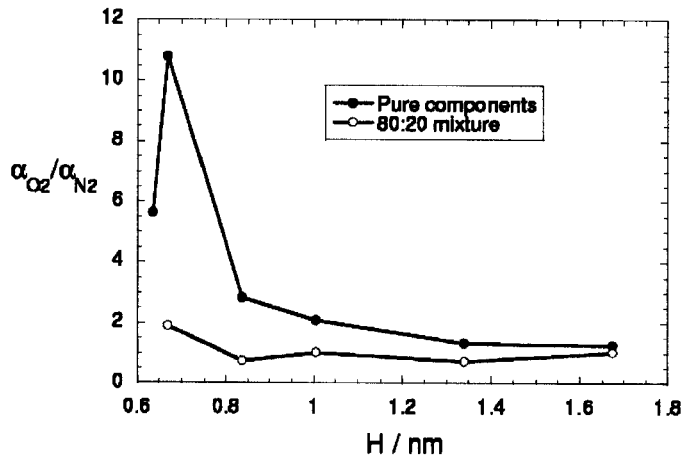

FIGURE 16 Plot of permselectivity (α_{O_2}/N_2) against pore width at $t = 25°C$. The filled symbols represent the permselectivity for the pure components while the open symbols represent the mixture permselectivity. Data obtained from DCV GCMD simulations (mixture results are taken from Ref. [5]).

2 at the lowest pore width studied. In the case of the pure components, oxygen selectivity is higher than in the mixture at all pore widths. The oxygen selectivity reaches a maximum value of about 11 at a pore width of 0.67 nm, exactly the same pore width at which the diffusive selectivity is a maximum for oxygen. At the lowest pore width studied, oxygen selectivity decreases, again mirroring the behaviour of the diffusive selectivity.

Possible Diffusion Mechanisms

Our results for the pure component diffusion have revealed a selectivity reversal at low pore widths. Clearly two different mechanisms give rise to these different regimes. The pore width below which oxygen becomes selective is 0.8375 nm. This pore width is wide enough (allowing for the dead space due to the carbon atoms in graphite) for both molecules to rotate about both axes. The length of a nitrogen molecule is 0.439 nm while that of an oxygen molecule is 0.411 nm. At the next lowest pore width (of physical width 0.67 nm), the nitrogen molecules would be unable to rotate about one of their axes. The oxygen molecules, while they could not rotate freely about the same axis, may still undergo large amplitude "frustrated" rotations. Using transition state theory, Singh and Koros [30] have shown that such a loss of rotational freedom in nitrogen can indeed lead to a drop in diffusivity relative to that of oxygen. We therefore postulate that such "entropic" effects are responsible for the selectivity observed at 0.67 nm. Below this pore width, oxygen will loose its "entropic" advantage at which point selectivity is based upon molecular size.

At 0.8375 nm, both diffusion coefficients are maximised but selectivity is now in favour of nitrogen. In order to understand this phenomenon, it is necessary to look at the behaviour of the intermolecular energy between a molecule and the graphite planes as a function of pore width. Average potential energies were obtained in a simulation by taking a single molecule and randomly translating and rotating it within the pore space such that the potential energy was averaged over all positions and orientations. Figure 17 shows the potential energy plotted as a function of the z-co-ordinate for the entire range of pore widths studied. What we notice from this figure is a substantial lowering of the potential barrier height for nitrogen at 0.8375 nm, compared to the higher pore widths. Figure 18 shows the 0.8375 nm pore width potentials in more detail. If molecules are to hop from one graphite plane to the opposing plane, they must have sufficient thermal energy to overcome this potential barrier. At pore widths lower than 0.8375 nm, molecules are trapped in a deep potential well between the two walls from which they cannot escape. Conditions at 0.8375 nm are optimum however for the wall to

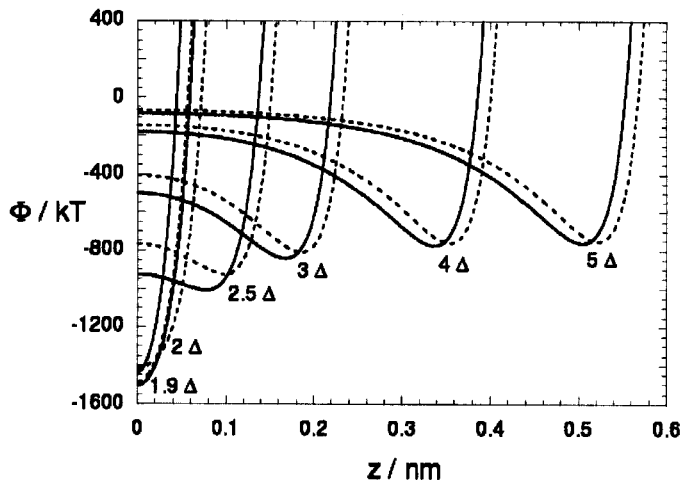

FIGURE 17 Plot of graphite-molecule intermolecular potential energy as a function of the z-coordinate (as the pore is symmetric we show only the positive values of z). The energy is plotted at six different pore widths for nitrogen (solid lines) and oxygen (broken lines).

wall hopping mechanism to occur. Beyond this pore width, the barrier heights are too great and the majority of the molecules spend most of their time trapped in the vicinity of one wall or another. This regime is then characterised by an energetic selectivity mechanism as opposed to the entropic selectivity mechanism in operation in pores less than or equal to 0.67 nm in width.

SUMMARY AND CONCLUSIONS

Using the industrial separation of air into its major constituents as a motivation we have undertaken a molecular simulation study of the mass transport of oxygen and nitrogen through graphite slit pores in a bid to understand the molecular origins of the reported kinetic oxygen selectivity. We have used both non-equilibrium molecular dynamics methods and equilibrium methods (Monte Carlo and molecular dynamics) in our study to extract the maximum information. The method of DCV GCMD has the advantage of enabling a direct calculation of permeability and permselectivity in a simulation that closely mimics gas flow though membranes under pressure and chemical potential gradients. The disadvantage of this method is that the diffusion coefficients are not easily obtained, particularly in the case of mixture diffusion. These limitations are offset by using the EMD and GCMC methods.

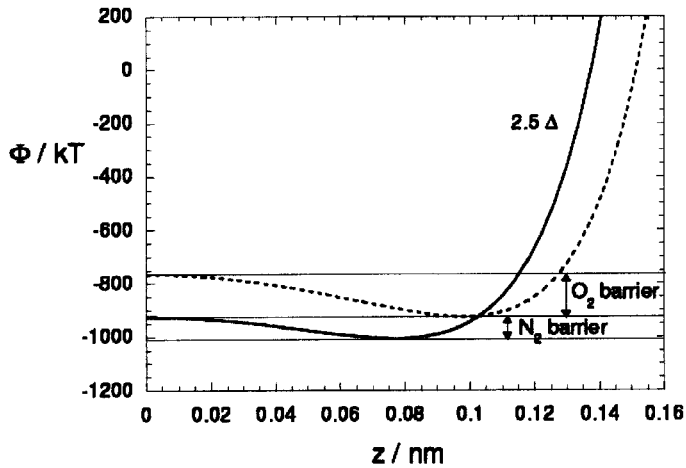

FIGURE 18 Plot of graphite-molecule intermolecular potential energy as a function of the z-coordinate (as the pore is symmetric we show only the positive values of z). The energy is plotted at a pore width of 0.83 75 nm to highlight the difference between the nitrogen (solid lines) and oxygen (broken lines) energies.

Our results show that a permselectivity in favour of oxygen is obtained across a range of pore widths for pure gas transport. This selectivity is significantly reduced when oxygen is present as the minor constituent in a mixture of oxygen and nitrogen at a composition similar to that in air. Furthermore, the permselectivity inverts at some pore widths to favour nitrogen. The permselectivity can be split into two contributions: a diffusive selectivity and a sorptivity selectivity. The latter quantity is a thermodynamic quantity that is related to the inverse slopes of the adsorption isotherms. Using GCMC we have explored the pore width and density dependence of the related quantity, the Darken factor, and found that the ratio of Darken factors is less than unity. Thus, the sorptivity favours nitrogen at all pore widths and densities studied, although the ratio becomes closer to unity at lower pore widths and may exceed it at yet lower pore widths. The other contribution to the permselectivity arises from the diffusivity ratio.

Using EMD we have been able to establish that viscous contributions to the intrapore flux are weak. These simulations established that the collective diffusivities. D_0, show an interesting pore width dependence. There are three diffusive regimes: A regime at pore widths in excess of 1 nm in which the diffusion coefficients show a weak pore width dependence at ambient temperature, a second regime at around 0.8375 nm where the diffusion coefficients increase, and a third regime at narrower pore widths where the diffusion coefficients decrease sharply. This latter regime is characterised by a

diffusive selectivity in favour of oxygen, which we believe to be an "entropic" effect in agreement with the findings of Singh and Koros [30]. This "entropic" effect arises in pores which are too narrow for the larger nitrogen molecules to rotate freely about both axes but not narrow enough to prevent the oxygen molecules from rotating about both axes. The sharp drop in the absolute values of the diffusivities below 1 nm corresponds to the adsorbate becoming a quasi-two-dimensional fluid; the slits are too narrow for more than one layer of molecules to form in the z-direction. These highly confined molecules are trapped in deep potential energy wells from which they cannot execute hopping motions. The lack of sensitivity of the diffusivities to pore width for the wider pores is a result of the molecules being tightly bound to the graphite surfaces. The barriers over which the molecules must hop to reach the alternative surface are too great at ambient temperature. These barrier heights do not significantly reduce until a pore width of 0.8375 nm is reached at which point the barrier for nitrogen is significantly lower than that of oxygen. This fact may explain why there is nitrogen selectivity at this pore width. At pore widths lower than 0.67 nm, the extra rotational degree of freedom possessed by the oxygen molecule is lost. Size selectivity then becomes important. The smaller oxygen molecules will diffuse faster than nitrogen but the absolute value will be low. At the lowest pore width we have studied, there is evidence of such an effect - oxygen is adsorbed more strongly than nitrogen at low pressures as a result of the nitrogen–graphite potential energy being shifted upwards as the repulsive energy begins to dominate. This marks the beginning of the molecular sieving regime.

The use of EMD simulations has allowed us to split the collective diffusivity into a self diffusivity, D_S, and a cross coupling diffusivity, D_ξ. We find that the self-diffusion contribution to the collective diffusion coefficient decreases as the pore width decreases. As pore width decreases, density increases. The trend in D_S with density follows closely the trend seen in bulk fluids. The cross coupling diffusivity, on the otherhand, varies with pore width, and begins to dominate the self diffusivity as the pore width narrows. This effect is not simply related to the density change. The cross coupling diffusivity is greater for nitrogen at pore widths larger than 0.67 nm and this cancels out any self diffusion selectivity in favour of oxygen. At lower pressures, where transport diffusion is dominated by self diffusion, higher oxygen selectivities will result while at higher pressures, dominated by cross coupling diffusivity, nitrogen selectivity will result unless the pore widths become so narrow that entropic effects work against nitrogen.

Our simulation study has revealed a rich behaviour of diffusion coefficients for oxygen and nitrogen in single slit pores. Real molecular sieving carbon (MSC) contains a distribution of pore widths. Typical MSC pore size distributions

display a maximum around 0.5 nm. Allowing for the excluded volume of the implicit carbon atoms in our slit pore model, the pores of width 0.8375 nm and lower correspond to typical pores found in MSC. In this regime of pore widths, we observe a large change in diffusion behaviour. High diffusivities at 0.8375 nm mean high fluxes albeit at the expense of oxygen selectivity. Lower pore widths favour oxygen selectivity but at the expense of greatly lowered absolute diffusivity and hence lower permeability. However, by lowering the pressure, both the absolute oxygen diffusivity and the oxygen selectivity can be improved since pressure has virtually no effect on the nitrogen diffusivity at the 0.67 nm pore width.

High oxygen selectivity for pure component flow does not necessarily translate to high selectivity in mixtures of gases. We have shown that the oxygen selectivity is severely reduced in the 80:20 mixtures. Furthermore, we have clearly demonstrated that the cross diffusion coefficients in mixtures are not insignificant and must therefore be taken into consideration in any model of mass transfer through membranes. A knowledge of the composition and pore width dependence of these cross diffusion coefficients and how they relate to the pure component diffusion coefficients is the subject of our future work.

Finally, we note that our simple model is unable to reproduce the large oxygen selectivities obtained in experimental studies of uptake in real molecular sieving carbons. The single slit pore model, whilst a very convenient and useful theoretical construction, is probably too crude to capture the real effects of a microporous carbon, where many adsorbate molecules will be in connections or at edges of microcrystals. Simulation results of gas transport through pores based on the randomly etched graphite pore model (REGP) of Seaton *et al.*[2] suggest that attention should be focussed towards studying transport of oxygen and nitrogen in more realistic microporous carbon models such as those generated via reverse Monte Carlo [31].

Acknowledgements

We are grateful to the National Science Foundation for the support of this work through research grant no. CTS-9908535; supercomputer time was provided through an NSF NRAC grant no. MCA93SOIIP).

References

[1] Chihara, K. and Suzuki, M. (1979) "Control of micropore diffusivities of molecular sieving carbon by deposition of hydrocarbons", *Carbon* **17**, 339.

[2] Seaton, N.A., Friedman, S.P., MacElroy, J.M.D. and Murphy, B.J. (1997) "The molecular sieving mechanism in carbon molecular sieves: a molecular dynamics and critical path analysis", *Langmuir* **13**, 1199.
[3] MacElroy, J.M.D., Friedman, S.P. and Seaton, N.A. (1999) "On the origin of transport resistances within carbon molecular sieves", *Chem. Engng Sci.* **54**, 1015.
[4] Travis, K.P. and Gubbins, K.E. (1999) "Transport diffusion of oxygen–nitrogen mixtures in graphite pores: a nonequilibrium molecular dynamics (NEMD) study", *Langmuir* **15**, 6050.
[5] Mason, E.A. and Viehland, L.A. (1978) "Statistical–mechanical theory of membrane transport for multicomponent systems: passive transport through open membranes", *J. Chem. Phys.* **68**, 3562.
[6] Mason, E.A. and Malinauskas, A.P. (1983) Gas Transport in Porous Media: The Dusty Gas Model (Elsevier, Amsterdam).
[7] MacElroy, J.M.D. (1996) Diffusion in Homogeneous Media in Diffusion in Polymers, Neogi, P., ed, (Marcel Dekker, New York).
[8] Karger, J. and Ruthven, D.M. (1992) Diffusion in Zeolites and other Microporous Solids (Wiley, New York).
[9] Nicholson, D. (1998) "Simulation studies of methane transport in model graphite micropores", *Carbon* **36**, 1511.
[10] Heffelfinger, G. and Swol, F.V. (1994) "Diffusion in Lennard–Jones fluids using dual control volume grand canonical moelcular dynamics simulation (DCV-GCMD)", *J. Chem. Phys.* **100**, 7548.
[11] MacElroy, J.M.D. (1994) "Nonequilibrium molecular dynamics simulation of diffusion and flow in thin microporous membranes", *J. Chem. Phys.* **101**, 5274.
[12] Cracknell, R.F., Nicholson, D. and Quirke, N. (1995) "Direct molecular dynamics simulation of flow down a chemical potential gradient in a slit-shaped micropore", *Phys. Rev. Lett.* **74**, 2463.
[13] Pohl, P.I., Heffelfinger, G.S. and Smith, D.M. (1996) "Molecular dynamics computer simulation of gas permeation in thin silicalite membranes", *Mol. Phys.* **89**, 1725.
[14] Ford, D.M. and Heffelfinger, G.S. (1998) "Massively parallel dual control volume grand canonical molecular dynamics with LADERA II. Gradient driven diffusion through polymers", *Mol. Phys.* **94**, 673.
[15] Travis, K.P. and Gubbins, K.E. (1998) Sixth Fundamentals of Adsorption (Elsevier, Amsterdam), pp 1161–1166.
[16] Nicholson, D. (1997) "The transport of adsorbate mixtures in porous materials: basic equations for pores with simple geometry", *J. Membr. Sci.* **129**, 209.
[17] Travis, K.P., Todd, B.D. and Evans, D.J. (1997) "Departure from Navier – Stokes, hydrodynamics in confined liquids", *Phys. Rev. E* **55**, 4288.
[18] Travis, K.P. and Gubbins, K.E. (2000) "Poiseuille flow of Lennard–Jones fluids in narrow slit pores", *J. Chem. Phys.* **112**, 1984.
[19] Travis, K.P. and Gubbins, K.E. (2000) "Combined diffusive and viscous transport of methane in a carbon slit pore", *Mol. Simul.* **25**, 209.
[20] Steele, W.A. (1974) The Interaction of Gases with Solid Surfaces (Pergamon Press, Oxford).
[21] Weiner, S.J., Kollman, P.A., Nguyen, D.T. and Case, D.A. (1986) "An all atom force field for simulation of proteins and nucleic acids", *J. Comput. Chem.* **7**, 230.
[22] Beenakker, J.J.M., Bonnan, V.D. and Krylov, S.Y. (1995) "Molecular transport in subnanometer pores: zero-point energy, reduced dimensionality and quantum sieving", *Chem. Phys. Letts.* **232**, 379.
[23] Kaneko, K., Cracknell, R.F. and Nicholson, D. (1994) "Nitrogen adsorption in slit pores at ambient temperatures: comparison of simulation and experiment", *Langmuir* **10**, 4606.
[24] Nose, S. (1984) "A unified formulation of the constant temperature molecular dynamics method", *J. Chem. Phys.* **81**, 511.
[25] Hoover, W.G. (1985) "Canonical dynamics—equilibrium phase-space distributions", *Phys. Rev. A* **31**, 1695.
[26] Alien, M.P. and Tildesley, D.J. (1987) Computer Simulation of Liquids (Oxford Science Publications, Oxford).
[27] Evans, D.J. and Morriss, G.P. (1990) Statistical mechanics of nonequilibrium liquids (Academic Press, London).

[28] Daivis, P.J., Evans, D.J. and Morriss, G.P. (1992) "Computer simulation study of the comparative rheology of branched and linear alkanes", *J. Chem. Phys.* **97**, 616.
[29] MacElroy, J.M.D. and Boyle, M.J. (1999) "Nonequilibrium molecular dynamics simulation of a model carbon membrane separation of CH_4/H_2 mixtures", *Chem. Engng J.* **74**, 85.
[30] Singh, A. and Koros, W. (1996) "Significance of entropic selectivity for advanced gas separation membranes", *J. Ind. Engng Chem. Res.* **35**, 1231.
[31] Tomson, K.T. and Gubbins, K.E. (2000) "Modeling structural morphology of microporous carbons by reverse Monte Carlo", *Langmuir* **16**, 5761.